Spectrally Resolved Longwave Surface Emissivity Reduces Atmospheric Heating Biases

L. Manzo[1], C. Zender[1], J. Tolento[1], and C. Whicker-Clarke[2]

[1]University of California, Irvine, Department of Earth System Science
[2]University of Michigan, Ann Arbor, Department of Climate and Space Sciences and Engineering

Key Points:

- Broadband surface emissivity assumptions combined with atmospheric conditions bias upwelling flux and heating rates in Earth system models.
- These assumptions tend to artificially cool Earth's surface and stabilize the lower troposphere.
- Longwave flux bias can be reduced by over 70% by updating broadband values, and by over 99.9% by a semi-spectral emissivity representation.

Corresponding author: Lili Manzo, `lmanzo1@uci.edu`

Abstract

Many Earth system models (ESMs) approximate surface emissivity as a constant. This broadband approximation reduces computational burden, yet biases longwave (LW) atmospheric fluxes and heating by neglecting the spectral structure of surface emissivity and atmospheric absorption. These biases are largest over surfaces with strongly varying emissivity and minimal atmospheric opacity (e.g., due to water vapor and clouds). Our study focuses on liquid water, ice, and snow surfaces. We use LW spectral emissivity $\epsilon(\lambda)$ calculated via the Fresnel equations and validated against a dataset of spectral surface emissivity. We flux-weight and bin $\epsilon(\lambda)$ into 16 spectral bands accepted by an offline single-column atmospheric radiative transfer model (RRTMG_LW) commonly used in ESMs (including E3SM and CESM). We quantify flux and heating biases introduced by broadband emissivity assumptions in comparison with the 16-band spectrally resolved case for three different surface types, three standard atmospheric profiles, and for the key drivers surface temperature, cloud water path, and atmospheric water vapor. In addition, we devise and test novel greybody and semi-spectral methods of representing $\epsilon(\lambda)$ with the goal of reducing biases while preserving computational efficiency. We find that typical broadband assumptions artificially cool Earth's surface, thereby stabilizing the lower troposphere. LW upwelling flux is overestimated by 4.5 W/m^2 ($\sim$1.4%) at the bottom of a mid-latitude winter atmosphere over an ice surface, and by 3.3 W/m^2 ($\sim$1.4%) at the top of atmosphere. Lastly, we find that a semi-spectral approach (five bands instead of 16) reduces biases by up to 99% relative to the broadband approximation.

Plain Language Summary

Earth's energy budget is controlled by the amount of incoming and outgoing radiation. Outgoing radiation has either been reflected or absorbed and emitted. The energy emitted by Earth is in part controlled by the emissivity $\epsilon(\lambda)$ of the surface. Emissivity depends on a variety of factors, notably wavelength and surface composition. Atmospheric energy absorption is also strongly wavelength dependent. However, many Earth system models (ESMs) currently employ a broadband assumption for surface emissivity, approximating $\epsilon(\lambda)$ as a constant. The broadband assumption introduces error, or bias, in the models' representation of outgoing radiation. This study quantifies the bias introduced by the broadband assumption by expanding the resolution of emissivity from one spectral bin to 16. We also devise and investigate novel methods of representing spectral emissivity that reduce bias and optimize computational resources. We find that eight or fewer bands are necessary to effectively eliminate LW flux and heating biases. Out of the cases we test, we find that the blackbody approximation can overestimate upwelling flux by up to 4.5 W/m^2 ($\sim$1.4%) at the bottom of atmosphere, and up to 3.3 W/m^2 ($\sim$1.4%) at the top of atmosphere.

1 Introduction

To predict the consequences of anthropogenic climate forcing, we must accurately depict Earth's energy budget. Earth cools via longwave (LW) energy emission. The surface emissivity modulates the amount of upwelling LW radiation that Earth emits. Emissivity ($\epsilon(\lambda)$) is defined as the ratio between actual emitted energy and idealized blackbody emission. It depends on a variety of factors including surface composition, temperature, and wavelength. The emissivity of a pure water surface, for example, varies by about 20% in the longwave regime. Feldman et al. (2014) show that variations in emissivity as small as 5% can impact outgoing radiation up to 2 W/m^2. However, Earth system models (ESMs) such as the Community Earth System Model (CESM) and Energy Exascale Earth System Model (E3SM) continue to approximate surface emissivity as constant blackbody ($\bar{\epsilon} = 1$) or greybody ($\bar{\epsilon} < 1$) over all wavelengths. This assumption helps to optimize model efficiency, since it reduces the amount of information passed be-

tween the surface components and the atmosphere. The broadband assumption also creates model biases, especially over water, ice, and snow surfaces, whose emissivities vary strongly with wavelength, and cover over 80% of Earth's surface. Atmospheric energy absorption also depends strongly on wavelength, from ∼7% near the atmospheric window up to 100% in the CO_2 absorption bands. Thus, the black- or greybody approximations decorrelate surface emission features from atmospheric absorption bands and fail to produce the true spectral and spatial patterns of surface cooling and atmospheric heating. The full effects of these approximations on climate prediction is unknown, though hinted at in previous studies.

Huang et al. (2016) implemented one month of global observations of surface emissivity and atmospheric conditions in an offline radiative transfer model. They found that top-of-atmosphere outgoing LW radiation decreases globally by up to 1.5 W/m^2 for a clear sky, and 0.9 W/m^2 for all-sky, in both January and July when comparing the spectrally resolved measured surface emissivity to the broadband assumption. A later study incorporated spectral surface emissivity in the atmospheric component of CESM without modifying surface components (Huang et al., 2018). Huang et al. (2018) found a global mean bias in upwelling LW flux over a 30-year time period of 1.00 ± 0.16 W/m^2 from a fully coupled run. They also found global mean surface temperature differences of 0.54 K from the coupled run as a result of their modifications when compared to the standard CESM that employs the broadband assumption, with some larger regional differences. Decreases in upwelling LW flux $F^{\uparrow}$ are typically balanced by increases in upwelling latent heat, which increases global precipitation. The largest reduction in LW flux bias appears over polar and desert regions, where water vapor concentrations are low. Huang et al. (2018) also uncovered a feedback loop between sea ice cover and surface emissivity which is similar to, but much weaker than, the well-known sea-ice albedo feedback. While previous work has quantified the impacts of spectrally resolved longwave emissivity in both offline and coupled atmosphere models, they have not coupled self-consistent spectral bands between the surface and atmosphere components.

This study uses first-principle methods to calculate emissivity over water, ice, and snow surfaces across the LW spectrum encompassed by the atmospheric radiative transfer model RRTMGP (10–3250 cm^{-1}, or 3.08–1000 μm), which is utilized by CESM and E3SM (Clough et al., 2004). We validate our calculations against the emissivity dataset developed by Huang et al. (2016) and implement spectrally resolved emissivity over water, ice, and snow surfaces in an offline atmospheric radiative transfer model. Other surface types such as desert and vegetation are omitted because their emissivities vary dramatically with season and location and are better represented empirically. We also investigate novel greybody and semi-spectral approximations with the goal of reducing biases while retaining computational efficiency if incorporated in a fully coupled ESM. We quantify the resulting changes in atmospheric radiative fluxes and warming rates for broadband versus spectrally-resolved surface emissivity over water, ice, and snow surfaces, three standard atmospheric profiles, and for varying surface temperature, cloud water path, and atmospheric water vapor. This work assesses the impacts of broadband surface emissivity assumptions and provides options for how to treat surface emissivity in fully coupled ESMs.

In Section 2, we describe the offline model, our methods for calculating $\epsilon(\lambda)$, and our various approaches to representing emissivity in the offline model. We present the results from the sensitivity tests of the broadband and semi-spectral approaches under different atmospheric conditions in Section 3. Finally, in Section 4 we discuss the implications of these results for future modifications to fully coupled ESMs.

2 Methods

2.1 Radiative transfer modelling

The RRTMGP radiative transfer model (Clough et al., 2004) is used by CESM and E3SM to calculate two-stream (upwelling and downwelling) radiation. RRTMG_LW is an offline single-column version of RRTMGP which provides instantaneous LW atmospheric fluxes and warming rates. RRTMGP_LW divides flux and emissivity into 16 spectral bands, ranging from 10–3250 cm^{-1}. RRTMG_LW has been validated against the Line By Line Radiative Transfer Model (LBLRTM), whose accuracy has been established by extensive comparison with atmospheric radiance measurements (Turner et al., 2004). Relative to LBLRTM, clear-sky flux and heating rate from RRTMG_LW are accurate within 1.5 W/m^2 and 0.4 K/d respectively at all atmospheric levels (Iacono et al., 2008).

The broadband surface emissivity varies between different models and even between different versions of the same ESM. For example, the sea-ice model in E3SM version 1 (Golaz et al., 2019) uses $\bar{\epsilon} = 0.95$ (Hunke & Lipscomb, 2010), while version 2 (v2) (Golaz et al., 2022) uses $\bar{\epsilon} = 1.0$ (E. Hunke, personal communication, 2023). In this study, we use the broadband values currently employed in E3SM v2: $\bar{\epsilon} = 1$ over the ocean, and 0.97 over land ice and snow (Oleson et al., 2013). CESM treats snow and ice surfaces in the same way (van Kampenhout et al., 2020). Because the v2 ocean is depicted as a blackbody, we use a calculated value of $\bar{\epsilon} = 0.94$ (described below) to explore greybody representations of emissivity over a water surface.

2.2 Calculating spectral emissivity

We use a dataset of refractive indices (Hale & Querry, 1973) to calculate the spectrally varying emissivity of pure water. We test four different methods over a water surface, shown in Figure 1. The calculation for ocean water is simplified by assuming a pure water surface. Liu et al. (1987) found that emissivity varies between fresh and sea water, as well as with varying concentrations of organic and inorganic sediment. However, the difference in emissivity between pure freshwater (0.978) and pure seawater (0.975) is negligible over the longwave spectrum examined in the study (8–14 μm). We apply the same methods to ice refractive indices from Warren and Brandt (2008) to calculate the spectral emissivity of an ice surface.

A surface emits energy at all angles, from zenith angle $\theta = 0°$ (perpendicular from surface) to $\theta = \pm 90°$ (parallel to surface). Emissivity that has been integrated and flux-weighed over all angles is diffuse emissivity, while emissivity at a single angle $\theta = \theta_0$ is direct. According to the diffusivity approximation constructed by Elsasser (1942), direct emissivity at $\theta_0 = 53°$ is close to the diffuse emissivity. This estimate is commonly employed for ease of computation and measurement (see Huang et al. (2016); Cheng et al. (2016)). We calculate diffuse emissivity following the method established by Briegleb and Light (2007), integrating over a resolution of 2000 angular grid points. Additionally, we calculate direct emissivity at $\theta = 53°$ following two different methods (Orfanidis, 2016; Liou, 2002) which both use Fresnel theory but differ slightly in their treatment of absorption. We also calculate hemispherically averaged emissivity as the multiplicative factor between blackbody and greybody upwelling flux (C. Zender, personal communication, 2023).

We validate the four different spectral emissivity calculations against the surface spectral emissivity dataset developed by Huang et al. (2016). Huang et al. (2016) developed the surface spectral emissivity dataset by modeling the direct surface emissivity of 11 surface types from 10–2000 cm^{-1} using the diffusivity approximation. These calculations are compared against satellite retrievals and in-situ measurements in the mid-infrared region (∼700–2700 cm^{-1}) to substantiate the model in the far-infrared (∼10–700 cm^{-1}) (Huang et al., 2016). We find that the method developed by Orfanidis (2016)

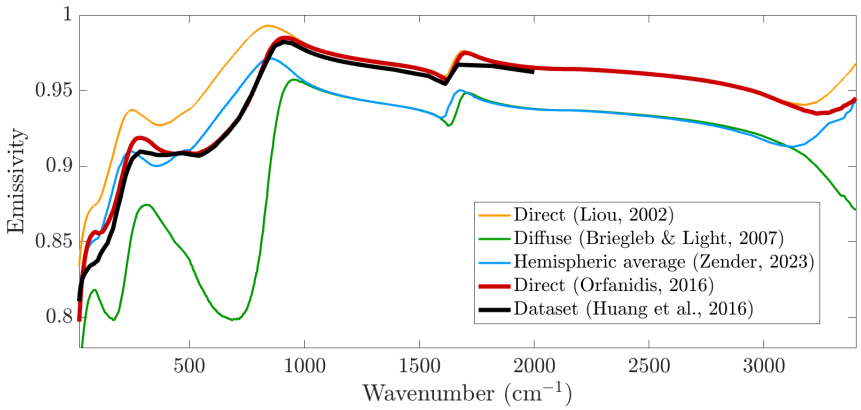

Figure 1. Spectral emissivity of a liquid water surface in the longwave regime calculated via four different methods: direct (yellow and red), diffuse (green), and hemispheric averaging (blue). We compare this to the emissivity of water obtained from the global dataset of spectral emissivity (black).

Table 1. Upwelling flux $F_{\mathrm{s}}^{\uparrow}$ from the surface model at temperature T_{s} and temperature T_{a} calculated and used by the atmospheric radiative transfer model RRTMG_LW for four methods of representing surface emissivity. We test $n = 2, 4, 5, 8$, and 16 spectral bins.

Method	$F_{\mathrm{s}}^{\uparrow}$	T_{a}
Blackbody	σT_{s}^4	$(F_{\mathrm{s}}^{\uparrow}/\sigma)^{1/4} = T_{\mathrm{s}}$
Effective greybody	$\bar{\epsilon}\sigma T_{\mathrm{s}}^4 + (1-\bar{\epsilon})F_{\mathrm{s}}^{\downarrow}$	$(F_{\mathrm{s}}^{\uparrow}/\sigma)^{1/4}$
Full greybody	$\bar{\epsilon}\sigma T_{\mathrm{s}}^4 + (1-\bar{\epsilon})F_{\mathrm{s}}^{\downarrow}$	$\left[\frac{F_{\mathrm{s}}^{\uparrow} - (1-\bar{\epsilon})F_{\mathrm{s}}^{\downarrow}}{\bar{\epsilon}\sigma}\right]^{1/4}$
Spectral (n-band)	$\pi \sum_{i=1}^{n} \epsilon_i \int_{\Delta\nu_i} B_\nu(T_{\mathrm{s}})\mathrm{d}\nu + \sum_{i=1}^{n}(1-\epsilon_i)F_i^{\downarrow}$	T_s

best agrees with the surface spectral emissivity dataset (Figure 1), and therefore we employ the Orfanidis (2016) method when calculating spectral emissivity for water and ice surfaces.

We follow the methods of Chen et al. (2014) and Huang et al. (2016) to model the emissivity of snow. These methods involve utilizing Mie theory to obtain the optical properties of snow. Due to snow's granular nature, the calculation of optical properties through Mie theory must be corrected via the static structure factor correction method (Mishchenko, 1994; Mishchenko & Macke, 1997; Wald, 1994). This accounts for changes in single-scattering properties among densely packed particles. Then, the Hapke emissivity model is applied to the scaled optical properties to calculate emissivity based on effective grain size. We use medium-grained snow, as it represents snow surfaces to an extent satisfactory to this study. Data provided by Feldman et al. (2014) extends from 10–3000 cm^{-1}; therefore, we extrapolate the final 250 cm^{-1} with a two-term exponential function $f(\nu) = -8.39\times 10^{-7}e^{0.00361\nu} + e^{-1.42\times10^{-5}\nu}$ fitted from wavenumber ν = 2400–2980 cm^{-1}, which has an R-squared value of 0.99999 (black dotted line, Figure 2).

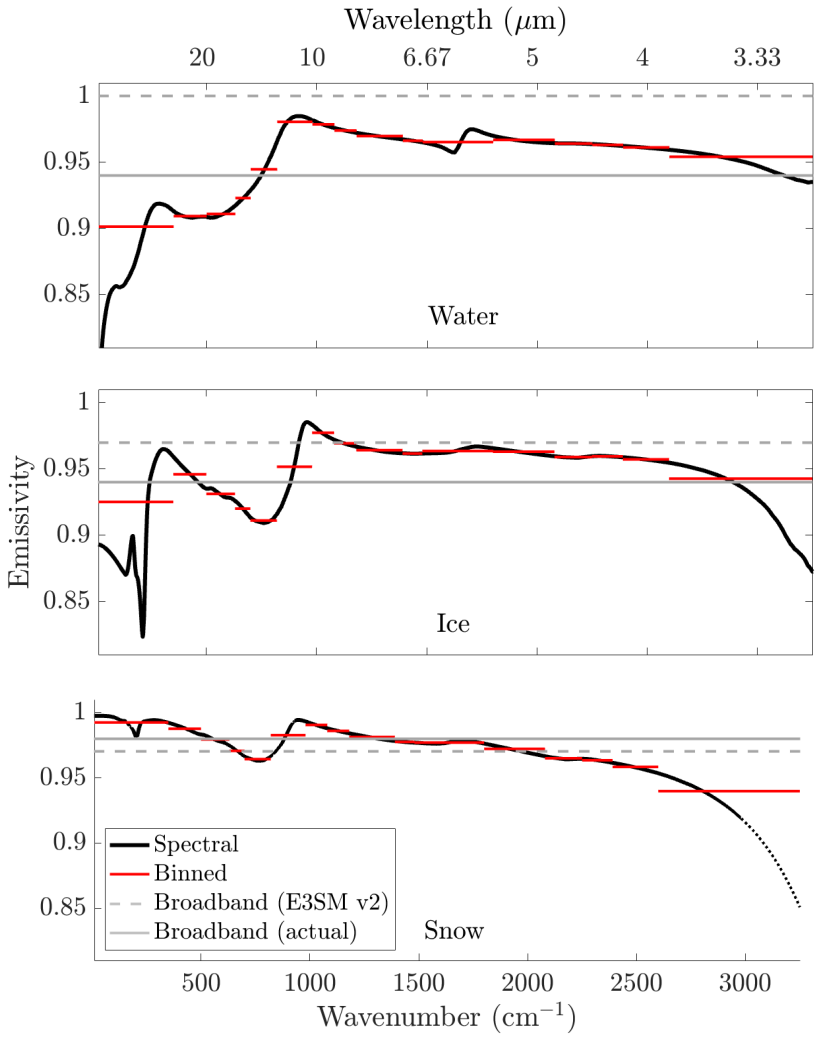

Figure 2. Spectral emissivity of water, ice, and snow surfaces in the longwave regime calculated via Fresnel theory (black). Emissivity is Planck-weighted by upwelling energy from a surface at temperature $T_s = 273$ K and partitioned in the 16 bins used by RRTMGP, shown in red. Current E3SM broadband assumptions are shown in dashed gray, and calculated (actual) broadband values are solid gray.

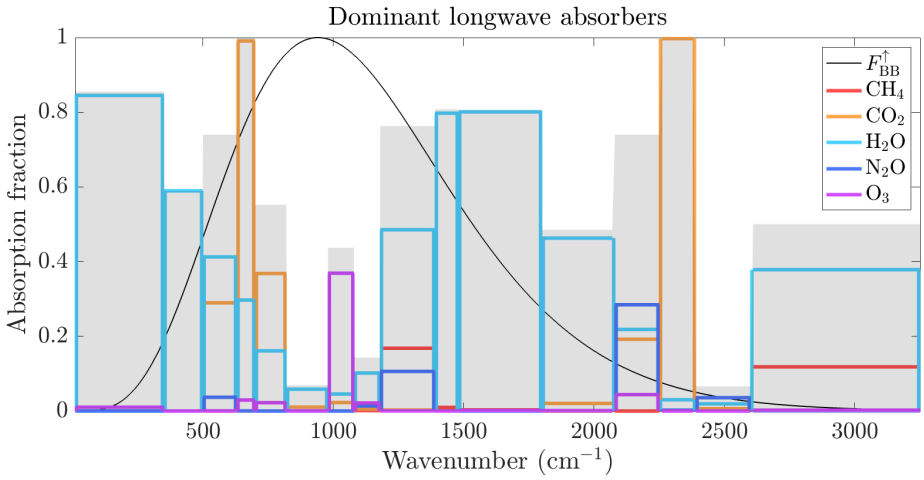

Figure 3. Fraction of longwave energy absorbed in the atmospheric column by the five strongest gaseous absorbers: methane (red), carbon dioxide (orange), water (light blue), nitrous oxide (dark blue), and ozone (magenta) (Zender, 1999), with blackbody emission $F^{\uparrow}_{\mathrm{BB}}$ from a surface at 273 K normalized and underlaid in black. Absorption fraction is binned and averaged over RRTMGP's 16 spectral bands. The gray shaded regions represent the sum of each gas's contribution to absorption, or total energy absorption fraction per band.

2.3 Implementing spectral and greybody emissivity in RRTMG_LW

2.3.1 Spectral emissivity

We use the Fresnel method of calculating emissivity over each band, as discussed in Section 2.2, to determine hyperspectral $\epsilon(\lambda)$ interpolated over a 1 cm^{-1} grid. We then bin $\epsilon(\lambda)$ by averaging and weighting the spectral emissivity by the flux upwelled by a blackbody at $T = 273$ K in each of RRTMGP's 16 bands. We replace the broadband constant $\bar{\epsilon}$ with this 16-band spectral emissivity in RRTMGP. The atmospheric fluxes obtained from this experiment are treated as the "true" or most accurate results to compare against all other methods. We quantify bias by normalizing the difference in flux per wavenumber from the broadband approximation ($F^{\uparrow}_{\mathrm{brb}}$) and the spectral case ($F^{\uparrow}_{\mathrm{spc}}$), then multiplying by $F^{\uparrow}_{\mathrm{brb}}$ to weigh by the amount of flux per band:

$$\Delta F^{\uparrow} = F^{\uparrow}_{\mathrm{brb}} \times \frac{F^{\uparrow}_{\mathrm{brb}} - F^{\uparrow}_{\mathrm{spc}}}{F^{\uparrow}_{\mathrm{spc}}}. \tag{1}$$

2.3.2 Semi-spectral emissivity

To completely eliminate the flux and heating biases, $F^{\uparrow}_{\mathrm{s}}$ must be spectrally resolved across RRTMGP's 16 bands. These 16 fluxes must then pass through the coupler to the atmosphere component, thereby increasing the required memory usage, bandwidth, and computational burden. Therefore, we additionally investigate bias from a variable n amount of bins which may efficiently eliminate bias. Efficiency can often be further improved when n evenly divides the number of CPU cores; therefore, we target cases $n = 2$, 4, and 8. We also include the five-band case as it exists near the juncture where flux bias approaches zero with increasing n. Starting with the 16-band case, we reduce n to 8 by combining the lower two (10–500 cm^{-1}) and upper eight (1180–3250 cm^{-1}) bands while preserving the middle six bands. The bin boundaries used in each method can be found in Ta-

ble 2. We combine the bins in this way based on the spectral distribution of upwelling flux as described by the Planck function. When $T_s = 273$ K, emitted flux peaks near 1000 cm^{-1}. Although there are significant absorption bands from H_2O, CO_2, and N_2O within the upper eight bands, they encompass only ∼5% of total upwelled flux, so bias is minimal in that region (see Figure 3). Though a larger fraction of LW flux is partitioned within the lower bands, flux found from the broadband approximation is very close to spectral and bias again is very low (about 6% of the total). We further reduce spectral resolution by expanding the ranges of the outer bands inwards towards 1000 cm^{-1}. We test this semi-spectral method over water, ice, and snow surfaces under a typical mid-latitude winter atmospheric profile, with surface temperature at 273 K where water can exist in both solid and liquid states.

2.3.3 Broadband emissivity

We test three different broadband approximations with $\bar{\epsilon}$, along with the spectral representation that discretizes $\epsilon(\lambda)$ into multiple bands, all summarized in Table 1. The first approximation assumes blackbody (BB) emission from the surface model, and blackbody emission at the same temperature in the atmosphere, with upwelling flux described by the Stefan-Boltzmann law $F^{\uparrow} = \sigma T_s^4$ where σ is the Stefan-Boltzmann constant and T_s is surface temperature. This approximation replicates the method used over E3SM's ocean and sea-ice models (MPAS-O and MPAS-SI, respectively), where $\bar{\epsilon} = 1$. The next approximation assumes greybody emission in the surface model and blackbody emission at the effective temperature of the total upwelling surface flux in the atmosphere. We call this the Effective Greybody (EG) approximation, which is used over the land model of E3SM (ELM) where $\bar{\epsilon} < 1$. Finally, we developed a third approximation which assumes greybody emission in the surface model and greybody emission at the same temperature in the atmosphere. We call this the Full Greybody (FG) approximation. The FG method is not currently implemented in ESMs. However, it may be more accurate than the BB or EG methods because it resolves the mismatch between T_a and T_s.

Currently in E3SM, the surface component passes one scalar broadband value for upwelling LW flux through the coupler to the atmosphere component. This flux $F_s^{\uparrow}$ is the sum of surface emission and reflection: $F_s^{\uparrow} = \bar{\epsilon}\sigma T_s^4 + (1-\bar{\epsilon})F_s^{\downarrow}$, where $F_s^{\downarrow}$ is downwelling LW flux at the surface and $\bar{\epsilon}$ is broadband emissivity. When the atmosphere model (EAM) receives $F_s^{\uparrow}$, it assumes a blackbody surface ($\bar{\epsilon} = 1$) to calculate an effective surface temperature:

$$T_{\text{eff}} = (F_s^{\uparrow}/\sigma)^{1/4}. \tag{2}$$

EAM then uses T_{eff} in RRTMGP to calculate atmospheric spectral fluxes in 16 spectral bands via the Planck function: $F_a^{\uparrow} = \pi \Sigma_{i=1}^{16} \int_{\Delta\nu_i} B(\nu, T_{\text{eff}}) \mathrm{d}\nu = \sigma T_{\text{eff}}^4$. It is during these steps that bias is introduced. Effective temperature is always lower than actual temperature, which leads to incorrect energy distribution by redshifting the Planck function per Wien's displacement law. The blackbody approximation avoids this discrepancy, and ensures that $T_s = T_a$ at the expense of a less accurate $\bar{\epsilon}$, and the neglect of any associated reflected flux. To quantify this bias in the offline model via the EG approximation, we run RRTMG_LW twice: once with a greybody surface at $T = T_s$, $\bar{\epsilon} = \epsilon_0$, and then with a blackbody surface at $T = T_{\text{eff}}$. The first run represents the calculation performed by the surface model, with the actual surface temperature and greybody emissivity. The second run then utilizes $F_s^{\uparrow}$ to calculate T_{eff} assuming $\bar{\epsilon} = 1$, using the effective surface temperature and blackbody emissivity to output fluxes equivalent to those partitioned by the atmosphere component.

The FG method simulates the effects of greybody emissivity in an ESM if the coupler were altered to pass an additional scalar for broadband greybody emissivity to the

Table 2. Spectral placement of bin boundaries b in cm^{-1} for a variable n amount of bins: spectral (n=16), semi-spectral (n=2, 4, 5, 8), and greybody (n=1).

n	10	350	500	630	700	820	980	1080	1180	1390	1480	1800	2080	2250	2390	2600	3250
16	b_1	b_2	b_3	b_4	b_5	b_6	b_7	b_8	b_9	b_{10}	b_{11}	b_{12}	b_{13}	b_{14}	b_{15}	b_{16}	b_{17}
8	b_1		b_2	b_3	b_4	b_5	b_6	b_7	b_8								b_9
5	b_1				b_2	b_3	b_4	b_5									b_6
4	b_1				b_2	b_3	b_4										b_5
2	b_1					b_2											b_3
1	b_1																b_2

atmosphere. This method also requires the atmosphere model to store downwelling flux $F_{\mathrm{s}}^{\downarrow}$ for one additional timestep. This alters Equation 2 in the following way:

$$T_{\mathrm{eff}} = T_{\mathrm{s}} = \left[\frac{F_{\mathrm{s}}^{\uparrow} - (1 - \bar{\epsilon}) F_{\mathrm{s}}^{\downarrow}}{\bar{\epsilon}\sigma} \right]^{1/4}. \tag{3}$$

FG ensures that atmospheric upwelling flux is computed at the exact temperature and emissivity as the surface model, rather than assuming a blackbody surface and effective temperature as in EG. We expect this method to reduce bias in upwelling flux with a minimal increase in computational expense, as it only requires one more scalar passed through the coupler and stored in memory.

2.4 Atmospheric profiles

We use atmospheric profiles from the InterComparison of Radiation Codes in Climate Models project (ICRCCM) (Ellingson & Fouquart, 1991; Ellingson et al., 1991) to demonstrate flux bias across three standard atmospheric states: tropical (TROP), mid-latitude winter (MLW), and sub-Arctic winter (SAW). These profiles are representative of typical conditions at their specified regions and seasons, allowing for a range of column water vapor paths (WVP) and surface temperatures (SAW: 257 K, 0.10 kg/m^2; MLW: 272 K, 8.4 kg/m^2; TROP: 300 K, 47.8 kg/m^2) which strongly impact LW radiation. We restrict surface types to the profiles where they are physically allowed: water when $T_{\mathrm{s}} \geq$ 273.16 K (TROP), ice and snow when $T_{\mathrm{s}} \leq 273.16$ K (MLW and SAW).

2.5 Single-parameter tests

We test the impacts that single parameters have on LW flux bias, varying surface temperature, column water vapor, cloud particle effective radius (r_{eff}), and cloud water path (CWP). We vary the temperature of an ice surface under sub-Arctic winter conditions from 190–270 K, from the coldest recorded SAW temperatures to near the melting point. Within a single layer of cloud in the troposphere (728 mb), we vary CWP from 0–100 g/m^2 and r_{eff} from 3–60 μm. To test the sensitivity to column water vapor, we simultaneously vary relative humidity from 0–100% of the maximum in every level, based on the local temperature and pressure. We utilize the tropical atmosphere profile where maximum WVP is 81.6 kg/m^2.

3 Results

3.1 Semi-spectral tests

We investigate a semi-spectral approach that combines bands which encompass the largest and smallest wavenumbers (Table 2), where we found the lowest levels of resolvable bias. With this approach, we test the bias remediated by two, four, five, and eight bands to assess the minimum number of bands needed to effectively eliminate flux bias. Bias (Equation 1) can be depicted in different ways. One way is to find the total bias by summing bias within each band (Figure 4 a, b, c), which can either be positive (flux is overestimated by the test case) or negative (flux is underestimated by the test case): $\Delta F_{\mathrm{tot}}^{\uparrow} = \sum_{i=1}^{16} \Delta F_i^{\uparrow}$. In this case, positive and negative spectral biases may cancel each other out, reducing total broadband bias. An alternative way is to treat the spectral biases as positive-definite, resulting in an absolute broadband bias: $\Delta F_{\mathrm{abs}}^{\uparrow} = \sum_{i=1}^{16} |\Delta F_i^{\uparrow}|$ (Figure 4 c, d, e). This bias is either equal to or greater than the total bias.

For a MLW liquid water surface (Figure 4 a, d), the magnitude of $\Delta F_{\mathrm{tot}}^{\uparrow}$ is similar to that of $\Delta F_{\mathrm{abs}}^{\uparrow}$, meaning that bias has the same sign in most spectral bands (in this case, mostly negative) and there is little cancellation. This means that reducing the amount

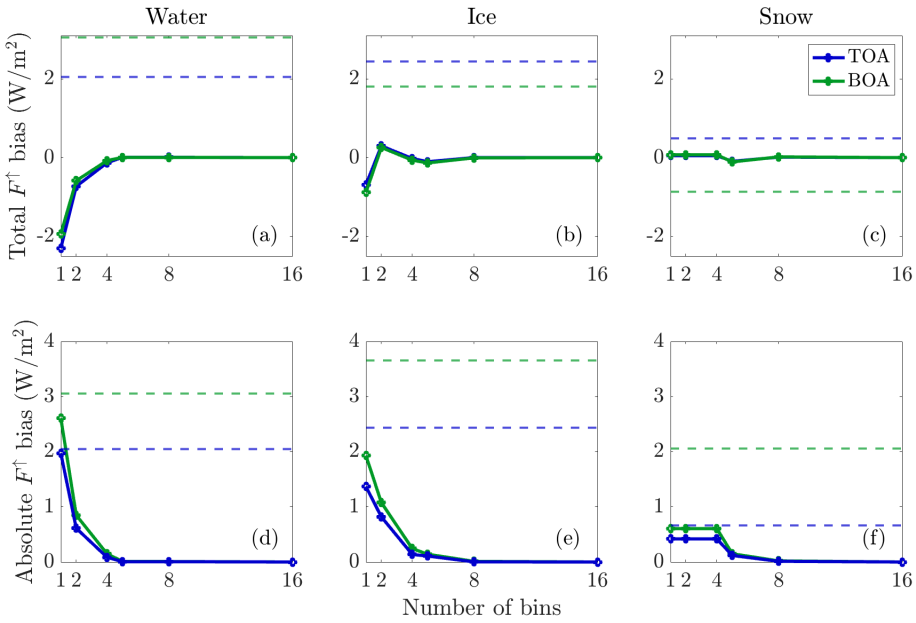

Figure 4. Total (top row) and absolute (bottom row) broadband bias of upwelling flux through the bottom- and top-of-atmosphere (green and blue respectively) as the number of spectral bins n increases. The atmospheric conditions are a typical mid-latitude winter over water (a, d), ice (b, e), and snow (c, f). Dashed lines illustrate the bias produced by the FG method utilizing current broadband assumptions employed in E3SM.

of spectral bins tends to increasingly underrepresent upwelling flux. However, for ice and snow (Figure 4 b, c, e, f), there is more variation in the flux bias sign. For example, it appears that using one, two, or four spectral bins over a snow surface produces smaller broadband bias than the five-band case when looking at the total bias. Yet $\Delta F^{\uparrow}_{\text{abs}}$ for the five-band case is significantly smaller than that of the lower band cases. One, two, and four spectral bands over a snow surface produce the same amount of bias because of the spectral shape of $\epsilon_{\text{snw}}(\lambda)$. The spectral emissivity of snow is flatter than that of water and ice, particularly in the middle bands (see Figure 2); greybody is reached at four bands, meaning further reduction of spectral resolution has no effect. Based on these results, it is clear that fewer than sixteen spectral bands suffice to nearly eliminate the flux and heating biases.

Furthermore, the biases produced by the current broadband approximations can be significantly reduced simply by improving the greybody ($n = 1$) value. Calculations of greybody emissivity via the Fresnel method used in this study find greybody values of 0.98 for snow, and 0.94 for ice and water (Figure 2). By changing the broadband emissivity to these calculated values, we can reduce $\Delta F^{\uparrow}_{\text{abs}}$ by 14.7% for water, 47.3% for ice, and 70.6% for snow at the bottom of a mid-latitude winter atmosphere.

3.2 Method intercomparison

We find that blackbody emissivity consistently overestimates upwelling flux over all tested surface types, because $\epsilon(\lambda) < 1$ for water, ice, and snow over the entire LW regime. The greybody assumption can bias $F^{\uparrow}$ either positively or negatively depending on the spectral bin, which reduces $F^{\uparrow}_{\text{tot}}$. In the case of a typical clear-sky mid-latitude winter atmosphere over an ice surface, for example, the blackbody assumption produces

Table 3. Total and absolute broadband bias in upwelling flux from the blackbody and greybody assumptions over an ocean surface through the top and bottom of atmosphere of a clear-sky tropical atmosphere. Percent of total upwelling flux is in parentheses. The smallest biases produced by a broadband approximation are bolded, and the method currently used in E3SM is italicized.

$\Delta F^{\uparrow}$ (W/m^2)	*Blackbody*	Effective greybody	Full greybody	Spectral 5
Total TOA	0.591 (0.20%)	**0.11 (0.04%)**	-0.766 (-0.27%)	0.011 (0.004%)
Total BOA	**1.69** (0.59%)	-1.96 **(0.43%)**	-1.96 **(-0.43%)**	0.021 (-0.005%)
Absolute TOA	0.591 (-0.20%)	**0.131 (-0.05%)**	0.766 (-0.27%)	0.011 (-0.004%)
Absolute BOA	**1.69** (-0.59%)	2.20 (-0.48%)	1.99 **(-0.44%)**	0.022 (-0.005%)

the largest bias by both total and absolute broadband metrics (Table 4). A five-band semi-spectral representation of surface emissivity is closest to the spectrally resolved case by over an order of magnitude (∼0.10 W/m^2). The total and absolute broadband biases for the four different emissivity approximations over a water surface under a tropical atmosphere, an ice surface under a mid-latitude winter atmosphere, and a snow surface under a sub-Arctic winter atmosphere, are summarized in Tables 3, 4, and 5, respectively.

While the semi-spectral method consistently produces the smallest bias in upwelling flux out of the four compared methods, the fidelity of the broadband approximations varies by surface type and atmospheric profile. For instance, for a sub-Arctic winter snow surface (Table 5), EG better represents $F^{\uparrow}$ at TOA, while FG is better at BOA. To further complicate matters, there is not always agreement between bias in irradiance versus percent of $F^{\uparrow}$. For example, both total and absolute BOA bias in W/m^2 over a tropical water surface are lowest via BB. However, in terms of upwelling flux fraction, EG and FG are tied. Interestingly, this shows that the blackbody approximation can be more accurate than either greybody method according to certain metrics in specific environmental conditions (Table 3). This is essentially happenstance, and in general the more physically based EG and FG broadband methods outperform BB.

A more detailed comparison of bias between the four methods is shown in Figure 5, weighted by bin size, with the same conditions as in Table 4. Spectrally, the largest biases are found near 1000 cm^{-1} (panel a, b), where $F^{\uparrow}$ is largest and $\epsilon(\lambda)$ deviates strongly from $\bar{\epsilon}$. Differences between BOA and TOA are caused by atmospheric absorption (Figure 3). Changes in surface emissivity negligibly alter downwelling flux $F^{\downarrow}$ (not shown). Absolute warming rate, $F^{\uparrow}$, $F^{\downarrow}$, and F^{net} for the same conditions as Figure 5 throughout the lower troposphere are provided in the supplementary material (Section 5, Figure 8). Overall, the broadband assumptions tend to overrepresent upwelling and net flux, artificially cooling most of the lower troposphere.

The mismatch between T_{eff} and T_{s} in the EG method (cf. Section 2.3.3) causes notable deviations in warming rate and LW fluxes in the lowest 100 mb of the atmosphere (panels c, d, e). Because T_{eff} is always less than T_{s}, the EG method artificially redshifts the peak energy emission (by 8.1 cm^{-1} in 5) per Wien's displacement law. This shifts more energy toward the strong CO_2 and H_2O absorption bands redward of 700 cm^{-1}, and causes the positively biased warming rate. This bias is strongest at the bottom of the atmosphere, where F^{up} and CO_2 and water vapor concentrations are all maximal.

3.3 Single-parameter sensitivity tests

The spatially limited nature of a single-column model prevents us from presenting a global view of flux biases incurred by LW broadband assumptions in ESM surface

Table 4. As in Table 3, for an ice surface and a mid-latitude winter atmosphere.

$\Delta F^{\uparrow}$ (W/m^2)	Blackbody	*Effective greybody*	Full greybody	Spectral 5
Total TOA	3.31 (1.4%)	2.39 (1.0%)	**1.28 (0.56%)**	-0.101 (-0.044%)
Total BOA	4.49 (1.4%)	**1.69 (0.55%)**	1.76 (0.57%)	-0.139 (-0.045%)
Absolute TOA	3.31 (1.4%)	2.40 (1.0%)	**1.43(0.63%)**	0.106 (0.046%)
Absolute BOA	4.49 (1.4%)	3.64 (1.2%)	**2.03 (0.66%)**	0.134 (0.044%)

Table 5. As in Table 3, for a snow surface and a sub-Arctic winter atmosphere.

$\Delta F^{\uparrow}$ (W/m^2)	Blackbody	*Effective greybody*	Full greybody	Spectral 5
Total TOA	1.29 (0.65%)	**0.436 (0.22%)**	-0.500 (-0.25%)	-0.078 (-0.039%)
Total BOA	1.61 (0.81%)	-0.703 (0.29%)	**-0.673 (-0.27%)**	-0.103 (-0.046%)
Absolute TOA	1.29 (0.65%)	**0.621 (0.31%)**	0.731 (0.37%)	0.092 (0.046%)
Absolute BOA	1.61 (0.81%)	1.67 (0.68%)	**0.958 (0.39%)**	0.122 (0.050%)

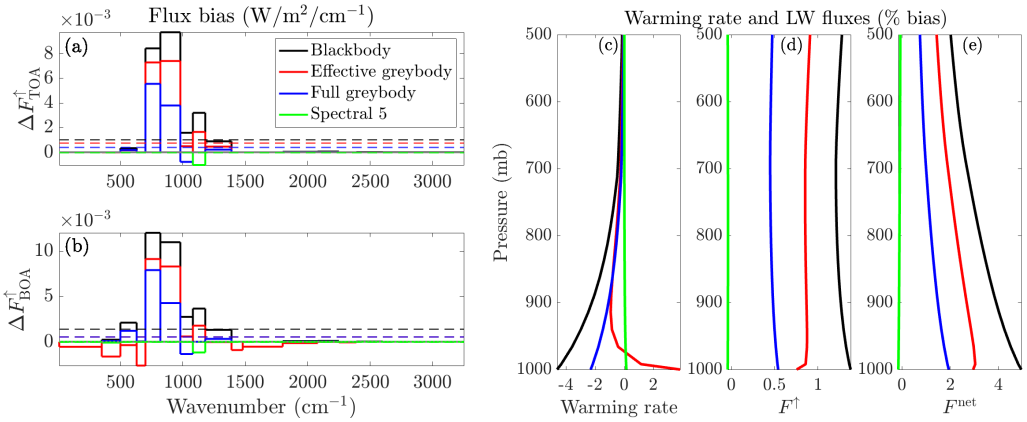

Figure 5. a) Distribution of top of atmosphere (TOA) upwelling spectral flux bias for blackbody emissivity (black), two greybody methods (red and blue), and the five-band semi-spectral method (green) of representing emissivity in relation to the spectral case through a clear-sky mid-latitude winter atmospheric profile over an ice surface. $F^{\uparrow}_{\mathrm{BB}}$ has been normalized to $F^{\uparrow}_{\mathrm{spc}}$ and weighed by band width. Dashed lines represent total broadband flux bias for each method. b) as in A, for bottom of atmosphere. c) Percent change in broadband warming rate throughout lower troposphere in relation to the spectrally resolved case. d) As in C, for upwelling LW flux. e) As in C, for net LW flux.

models. The cases we present above, with varying surface types and atmospheric profiles, demonstrate a diverse yet limited view of the ways in which the broadband surface emissivity assumption introduces bias to LW flux. Temperature, pressure, and atmospheric gas concentrations all vary simultaneously among the profiles. To provide a more continuous view of how these changing variables affect our results, here we investigate the magnitude of flux bias introduced by four fields with potentially the greatest effects on LW flux: surface temperature T_s, column vapor path (CVP), cloud water path (CWP), and cloud particle effective radius (Figure 6). Additionally, we examine bias sensitivity to the three surfaces types explored in this study (Figure 7). We use E3SM's current broadband values of $\bar{\epsilon} = 1$ over a water surface and $\bar{\epsilon} = 0.97$ over ice.

The upwelling LW broadband flux above a greybody surface is

$$F^{\uparrow}_{\mathrm{gb}} = \bar{\epsilon}\sigma T_\mathrm{s}^4 + (1-\bar{\epsilon})F^{\downarrow}_\mathrm{s} \tag{4}$$

where the first term is surface emission and the second term is reflected downwelling flux. The bias incurred by employing the blackbody approximation to a perfect greybody surface is the difference between upwelling blackbody flux ($F^{\uparrow}_{\mathrm{bb}} = \sigma T_\mathrm{s}^4$) and greybody flux (Equation 4), or

$$\Delta F^{\uparrow}_{\mathrm{gb}} = \sigma T_\mathrm{s}^4 - [\bar{\epsilon}\sigma T_\mathrm{s}^4 + (1-\epsilon)F^{\downarrow}_\mathrm{s}] = (1-\bar{\epsilon})(\sigma T_\mathrm{s}^4 - F^{\downarrow}_\mathrm{s}). \tag{5}$$

To quantify the bias of a broadband approximation relative to a fully spectral (16-band) representation, we must employ the discretized forms of $F^{\uparrow}_{\mathrm{gb}}$ and spectral flux $F^{\uparrow}_{\mathrm{spc}}$:

$$F^{\uparrow}_{\mathrm{gb}} = \bar{\epsilon}\pi \sum_{i=1}^{16} \int_{\Delta\nu_i} B_\nu(T_\mathrm{s})\mathrm{d}\nu + (1-\bar{\epsilon}) \sum_{i=1}^{16} F^{\downarrow}_{\mathrm{s},i} \tag{6}$$

and

$$F^{\uparrow}_{\mathrm{spc}} = \pi \sum_{i=1}^{16} \epsilon_i \int_{\Delta\nu_i} B_\nu(T_\mathrm{s})\mathrm{d}\nu + \sum_{i=1}^{16} (1-\epsilon_i) F^{\downarrow}_{\mathrm{s},i} \tag{7}$$

where $F^{\uparrow}_{\mathrm{spc}}$ is 16-band upwelling spectral flux, $B_\nu(T_\mathrm{s})$ is the Planck function, $F^{\downarrow}_{\mathrm{s},i}$ and ϵ_i are the downwelling BOA flux and emissivity of band i respectively, and $\Delta\nu$ is the range of wavenumbers spanned by the band (Huang et al., 2018). The bias $\Delta F^{\uparrow}$ from applying greybody approximation to a surface with spectrally varying emissivity is $F_{\mathrm{gb}} - F_{\mathrm{spc}}$, or

$$\Delta F^{\uparrow} = \left(\bar{\epsilon}\pi \sum_{i=1}^{16} \int_{\Delta\nu} B_\nu(T_\mathrm{s})\mathrm{d}\nu - \pi \sum_{i=1}^{16} \epsilon_i \int_{\Delta\nu} B_\nu(T_\mathrm{s})\mathrm{d}\nu \right) + \left(\bar{\epsilon} \sum_{i=1}^{16} F^{\downarrow}_{\mathrm{s},i} - \sum_{i=1}^{16} \epsilon_i F^{\downarrow}_{\mathrm{s},i} \right). \tag{8}$$

For ice and water surfaces, the broadband emissivities $\bar{\epsilon}$ employed in this study are greater than or equal to ϵ_i in every band besides ϵ_7 of ice (see Figure 2). Therefore, the error in the approximated emission, which is the difference between the first two terms on the right hand side, is positive definite. The error in approximated reflectance, the difference between the third and fourth terms, is also positive definite. The signs of the terms show that $\Delta F^{\uparrow}$ is positively correlated with surface temperature and negatively correlated with downwelling LW flux. This is demonstrated in Figure 6, which shows an increase in bias as T_s rises, and a reduction in bias as $F^{\downarrow}_i$ increases with CWP and CVP.

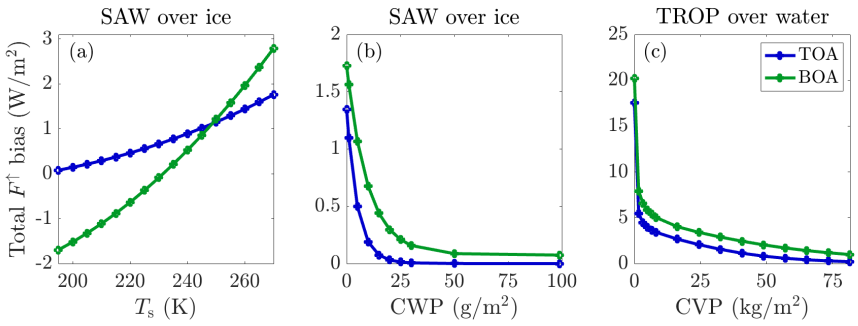

Figure 6. Single-parameter sensitivity tests over varying surface temperature T_s, cloud water path (CWP), and column vapor path (CVP). Total broadband bias in upwelling flux through the bottom of atmosphere (blue) and top of atmosphere (green) is shown.

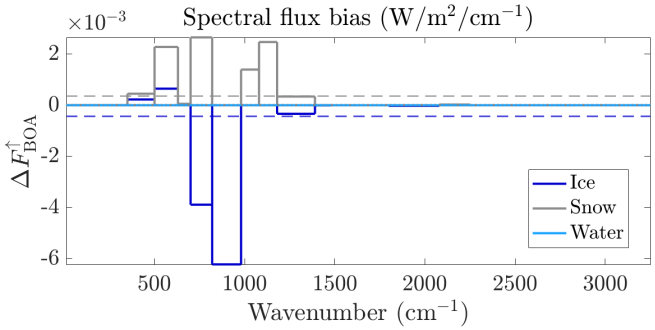

Figure 7. Spectral upwelling LW flux bias at the bottom of atmosphere over ice and snow surfaces compared to water under a mid-latitude winter profile at $T_s = 273$ K.

Bias follows an exponential decrease as CWP and CVP increase, in accordance with the Bouguer-Lambert law $I = I_0 e^{-\mu d}$ where μ is optical density and d is path length. The sharp rise in bias below ~3 kg/m^2 CVP demonstrates how quickly the major water vapor absorbance bands saturate. We find that cloud particle effective radius has no notable effect on flux bias for opaque clouds. The largest instantaneous radiative biases from current broadband approximations are therefore over regions with low moisture and cloud cover, in agreement with results from Huang et al. (2016, 2018).

Surface type itself also has an impact on forcing. Figure 7 compares forcing between water, ice, and snow surfaces by subtracting the spectral flux of a water surface under a MLW atmosphere at $T_s = 273$ K (the triple point of water) from the three surface types in identical atmospheric conditions. As such, the total broadband forcing from ice and snow at BOA are -1.25 and 1.15 W/m^2 with respect to a water surface. These instantaneous BOA forcings are expected to occur due to ice or snow melt. Fusion of liquid is expected to heat the resulting ice surface by +1.25 W/m^2.

4 Discussion and conclusions

We implemented spectrally resolved surface emissivity into a single-column offline radiative transfer model to quantify the biases introduced in ESMs such as E3SM via broadband assumptions. We also devised and implemented a novel method of representing greybody emissivity ("FG") and found that it reduces biases in certain conditions. Optimal broadband method depends on surface type, atmospheric state, and metric of

comparison. Over a tropical ocean surface, EG is the best method to represent $\Delta F^{\uparrow}_{\mathrm{TOA}}$; BB is best at $\Delta F^{\uparrow}_{\mathrm{BOA}}$ in Watts per square meter; and FG is best at $\Delta F^{\uparrow}_{\mathrm{BOA}}$ in flux fraction (Table 3). Interestingly, column bias in warming rate produced by the EG method is partially compensated by heightened absorption as a result of redshifted energy emission.

We examined three homogeneous surface types (water, ice, and snow) whose spectral emissivities can be accurately simulated from first principles, and whose current representation produces tractable biases and cover more than 80% of Earth's surface. Flux biases at the tops and bottoms of standard tropical, sub-Arctic winter, and mid-latitude winter atmospheric profiles due to broadband and semi-spectral assumptions were evaluated. We also quantified the extent to which surface temperature, cloud water path, column water vapor, and surface type impact upwelling LW flux bias. Variations in surface temperature from 195–270 K introduce biases in the broadband assumption from -1.7–2.8 W/m^2 at BOA. Cloud water path reduces bias by about 1.3 W/m^2 at TOA as it reaches saturation, while water vapor content impacts bias by up to 17.3 W/m^2 at TOA.

While full spectral emissivity (16-bands for RRTMGP) is ideal, we also investigated bias reduction with two, four, five, and eight bands. We found that a single change in the greybody value reduces current biases in E3SM by over 70%, and a five-band approximation of spectral emissivity reduces biases by over 99.9%. This method effectively eliminates biases while significantly reducing the computational burden of a full 16-band emissivity.

The blackbody approximation consistently over-represents emitted energy, or overcools Earth's surface, while greybody emissivity can over- or under-represent cooling depending on greybody value and method. Artificial cooling of the atmosphere due to $T_{\mathrm{eff}} < T_{\mathrm{s}}$ impacts global circulation and unrealistically reduces atmospheric warming rates, thereby stabilizing the lower troposphere. Related work which quantifies bias in shortwave (SW) atmospheric fluxes has found that the current ESM (e.g., E3SM and CESM) two-band representations of SW surface albedo $\alpha(\lambda)$ tend to overestimate surface and atmospheric heating, and artificially destabilize the lower troposphere (Tolento et al., accepted, 2023). However, this does not negate the biases introduced by the broadband emissivity assumption shown in this study because the SW and LW radiative processes that heat and cool Earth's atmosphere operate with distinct spatio-temporal characteristics. For example, Tolento et al. (accepted, 2023) find smaller SW biases over water surfaces compared to ice and snow, opposite to LW biases studied here. The spectral albedo of water has far less variance compared to spectral emissivity, making the two-band albedo approximation more precise. As a result, the cooling effects demonstrated in this study outweigh the heating effects of two-band albedo over water surfaces. Furthermore, emissivity-induced biases operate continually, whereas albedo-induced biases occur only during daylit hours.

Spectrally resolving $\epsilon(\lambda)$ or $\alpha(\lambda)$ alone may not improve climate simulations. Improved spectral representations of both surface emissivity and albedo should be implemented to avoid introducing new compensating biases. Work is currently underway to implement and assess the impacts of spectral emissivity and albedo in E3SM. While these changes necessitate increased computational burden and coupler bandwidth, in return they will improve surface and lower tropospheric heating, with effects that will propagate throughout the climate system.

5 Supplementary material

Warming rates and longwave fluxes in absolute values (K/day and W/m^2) from the Blackbody, Effective Greybody, Full Greybody, and Spectral 5 methods over an ice surface through a mid-latitude winter can be found in Figure 8.

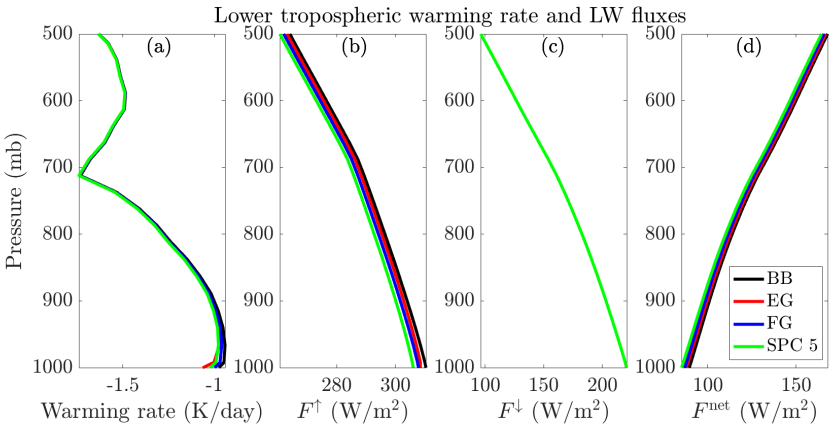

Figure 8. Absolute warming rate and longwave fluxes from four methods of representing emissivity of an ice surface through a MLW atmosphere.

6 Open research

The global database of surface spectral emissivity developed by Huang et al. (2016) can be found at `https://huang.engin.umich.edu/182-2/`. The offline radiative transfer model RRTMG_LW and the atmospheric profiles used in this study are available for download at `https://github.com/AER-RC/RRTMG_LW`. The MATLAB toolbox with the `fresnel` function used to calculate spectral LW emissivity can be accessed at `http://eceweb1.rutgers.edu/~orfanidi/ewa/`.

Acknowledgments

L. Manzo, C. Zender, and J. Tolento gratefully acknowledge support from the Energy Exascale Earth System Model project (DE-SC0022117) funded by the US Department of Energy, Office of Science, Biological and Environmental Research Program. C. Whicker gratefully acknowledges support from NSF Grant DGE 1841052. We also thank Xianglei Huang for his spectral emissivity dataset and help with emissivity estimates.

References

Briegleb, B. P., & Light, B. (2007, February). *A Delta-Eddington multiple scattering parameterization for solar radiation in the sea ice component of the Community Climate System Model* (Tech. Rep.). Boulder, CO: National Center for Atmospheric Research.

Chen, X., Huang, X., & Flanner, M. G. (2014). Sensitivity of modeled far-IR radiation budgets in polar continents to treatments of snow surface and ice cloud radiative properties. *Geophysical Research Letters*, *41*, 6530–6537. doi: 10.4137/CCRPM.S6882

Cheng, H., Chen, X., & Huang, X. (2016). Quantification of the errors associated with the representation of surface emissivity in the RRTMG_LW. *Journal of Quantitative Spectroscopy & Radiative Transfer*, *180*, 167–176. doi: 10.1016/j.jqsrt.2016.05.004

Clough, S. A., Shephard, M., Mlawer, E. J., Delamere, J. S., Iacono, M. J., Cady-Pereira, K., ... Brown, P. (2004). Atmospheric radiative transfer modeling: a summary of the AER codes. *Journal of Quantitative Spectroscopy & Radiative Transfer*, *91*, 233-244. doi: 10.1016/j.jqsrt.2004.05.058

Ellingson, R. G., Ellis, J., & Fels, S. (1991). The intercomparison of radiation codes used in climate models: Long wave results. *Journal of Geophysical Research*, *96*(D5), 8929. Retrieved 2023-01-23, from `http://doi.wiley.com/10.1029/90JD01450` doi: 10.1029/90JD01450

Ellingson, R. G., & Fouquart, Y. (1991). The intercomparison of radiation codes in climate models: An overview. *Journal of Geophysical Research*, *96*(D5), 8925. Retrieved 2023-01-23, from `http://doi.wiley.com/10.1029/90JD01618` doi: 10.1029/90JD01618

Elsasser, W. M. (1942). *Heat transfer by infrared radiation in the atmosphere.* Cambridge, MA: Harvard University.

Feldman, D. R., Collins, W. D., Pincus, R., Huang, X., & Chen, X. (2014). Far-infrared surface emissivity and climate. *Proceedings of the National Academy of Sciences*, *111*, 16297–16302. doi: 10.1073/pnas.1413640111

Golaz, J.-C., Caldwell, P. M., Roekel, L. P. V., Petersen, M. R., Tang, Q., Wolfe, J. D., ... Zhu, Q. (2019). The DOE E3SM coupled model version 1: Overview and evaluation at standard resolution. *Journal of Advances in Modeling Earth Systems*, *11*. doi: 10.1029/2018MS001603

Golaz, J.-C., Roekel, L. P. V., Zheng, X., Roberts, A. F., Wolfe, J. D., Lin, W., ... Bader, D. C. (2022). The DOE E3SM model version 2: Overview of the physical model and initial model evaluation. *Journal of Advances in Modeling Earth Systems*, *11*. doi: 10.1029/2022MS003156

Hale, G. M., & Querry, M. R. (1973). Optical constants of water in the 200-nm to 200-mm wavelength region. *Applied Optics*, *12*, 555-563.

Huang, X., Chen, X., Flanner, M., Yang, P., Feldman, D., & Kuo, C. (2018). Improved representation of surface spectral emissivity in a global climate model and its impact on simulated climate. *American Meteorological Society*, *31*, 3711–3727. doi: 10.1175/JCLI-D-17-0125.1

Huang, X., Chen, X., Zhou, D., & Liu, X. (2016). An observationally based global band-by-band surface emissivity dataset for climate and weather simulations. *American Meteorological Society*, *73*, 3541–3555. doi: 10.1175/JAS-D-15-0355.1

Hunke, E. C., & Lipscomb, W. H. (2010, May). *CICE: the Los Alamos sea ice model documentation and software user's manual version 4.1* (Tech. Rep.). Los Alamos, NM: Los Alamos National Laboratory.

Iacono, M. J., Delamere, J. S., Mlawer, E. J., Shephard, M. W., Clough, S. A., & Collins, W. D. (2008). Radiative forcing by long-lived greenhouse gases: Calculations with the AER radiative transfer models. *Journal of Geophysical Research: Atmospheres*, *113*. doi: 10.1029/2008JD009944

Liou, K. N. (2002). *An introduction to atmospheric radiation.* San Diego, CA: Elsevier Science.

Liu, W.-Y., Field, R. T., Gantt, R. G., & Klemas, V. (1987). Measurement of the surface emissivity of turbid waters. *Remote Sensing of Environment*, *21*, 97-109.

Mishchenko, M. I. (1994). Asymmetry parameters of the phase function for densely packed scattering grains. *Journal of Quantitative Spectroscopy and Radiative Transfer*, *52*, 91-110. doi: 10.1016/0022-4073(94)90142-2

Mishchenko, M. I., & Macke, A. (1997). Asymmetry parameters of the phase function for isolated and densely packed spherical particles with multiple internal inclusions in the geometric optics limit. *Journal of Quantitative Spectroscopy and Radiative Transfer*, *57*, 767-794. doi: 10.1029/97JD00237

Oleson, K. W., Lawrence, D. M., Bonan, G. B., Drewniak, B., Huang, M., Koven, C. D., ... Thornton, P. E. (2013, July). *Technical description of version 4.5 of the Community Land Model (CLM)* (Tech. Rep.). Boulder, CO: National Center for Atmospheric Research.

Orfanidis, S. J. (2016). *Electromagnetic waves and antennas.* New Brunswick, NJ:

Rutgers University.

Tolento, J. P., Zender, C. S., & Whicker, C. A. (accepted, 2023). Surface and atmospheric heating responses to spectrally resolved albedos of frozen and liquid water surfaces. *Journal of Geophysical Research*.

Turner, D. D., Tobin, D. C., Clough, S. A., Brown, P. D., Ellingson, R. G., Mlawer, E. J., ... Shephard, M. W. (2004). The QME AERI LBLRTM: A closure experiment for downwelling high spectral resolution infrared radiance. *Journal of the Atmospheric Sciences*, *61*. doi: 10.1175/JAS3300.1

van Kampenhout, L., Lenaerts, J. T. M., Lipscomb, W. H., Lhermitte, S., Noël, B., Vizcaíno, M., ... van den Broeke, M. R. (2020). Present-day Greenland ice sheet climate and surface mass balance in CESM2. *Journal of Geophysical Research: Earth Surface*, *125*. doi: 10.1029/2019JF005318

Wald, A. E. (1994). Modeling thermal infrared reflectance spectra of frost and snow. *Journal of Geophysical Research*, *99*. doi: 10.1029/94JB01560.

Warren, S. G., & Brandt, R. E. (2008). Optical constants of ice from the ultraviolet to the microwave: A revised compilation. *Journal of Geophysical Research*, *113*. doi: 10.1029/2007JD009744

Zender, C. S. (1999). Global climatology of abundance and solar absorption of oxygen collision complexes. *Journal of Geophysical Research*, *104*, 24,471-24,484. doi: 10.1029/1999JD900797